



Glasses in the NaPO₃-WO₃-NaF ternary system: preparation, physical properties and structural studies



Joao F.V.L. Munhoz^{a,b}, Silvia Helena Santagneli^a, Marcos de Oliveira Jr.^c, Ana Candida Martins Rodrigues^d, Hellmut Eckert^{c,e,*}, Marcelo Nalin^{a,**}

^a Chemistry Institute, São Paulo State University – UNESP, Araraquara, SP, Brazil

^b Chemistry Department, Federal University of São Carlos -UFSCar, São Carlos, SP, Brazil

^c São Carlos Institute of Physics, University of São Carlos -USP, São Carlos, SP, Brazil

^d Department of Materials Engineering, Federal University of São Carlos -UFSCar, São Carlos, SP, Brazil

^e Institut für Physikalische Chemie, Westfälische Wilhelms-Universität Münster, Münster, Germany

ARTICLE INFO

Keywords:

Phosphate glasses
Ionic conductivity
Mixed conductivity
Glass structure
Tungsten glasses

ABSTRACT

Oxyfluoride glasses with composition x WO₃ - 30 NaPO₃ - (70- x) NaF, with $30 \leq x \leq 70$ were prepared by melt-quenching and characterized with respect to their bulk physical properties and ionic conductivities. As the NaF content increases, the glass transition temperature, T_g , decreases systematically. Impedance measurements reveal no clear effect of NaF content upon room temperature electrical conductivities and activation energies. There is, however, a significant decrease of the Arrhenius pre-exponential factor with increasing WO₃ content, suggesting that the electrical conductivities measured in this glass series are increasingly influenced by an electronic contribution. This contribution may be related to a $W^{5+} \rightarrow W^{6+}$ electron hopping process detected in the optical absorption spectra. Detailed spectroscopic investigations by Raman scattering and multinuclear one- and two-dimensional solid-state NMR experiments indicate that NaF acts like a network modifier resulting in the formation of W-F bonds via breakage of W-O-W and W-O-P linkages, with the former process being the preferred one. The concomitant decrease in network connectivity caused by these processes accounts for the experimentally observed decrease in glass transition temperatures with increasing NaF contents.

1. Introduction

With a plethora of uses ranging from the domestic realm to high-end technologies glasses are not only pervading all aspects of our everyday life but are at the forefront of fundamental and applied research and development. For transforming a promising solid material into a functional device, many of its physical properties need to be optimized simultaneously. In this respect, glasses offer a vast parameter space for *fine-tuning* a material to its desired application, as their physical properties can be varied over wide ranges by adjusting their composition and processing parameters. Tungsten oxide containing phosphate glasses are of great interest because of their high glass transition temperatures, their superior hydrolytic stability compared to alkali phosphate glasses, their ability to host large concentrations of rare-earth ion emitters, and because of their special photochromic properties [1–11]. A highly desired property of these glasses would be their functionalization for ion transport, with potential applications in photoelectrochemistry, and as sensors in electrophysiology and optogenetics

[12–15]. This objective can be achieved by adding metal halide salt compounds to the glass formulation. To rationalize the concomitant changes in physical properties on the basis of a structural model, suitable spectroscopic techniques such as Raman scattering, EXAFS and solid-state NMR may be employed. In the present study we investigate the effect of NaF upon the bulk physical properties and the ionic conductivity of NaPO₃-WO₃ glasses, along the composition line x WO₃-30 NaPO₃ - (70- x) NaF ($30 \leq x \leq 70$). Based on a comprehensive structural characterization by multinuclear NMR and Raman spectroscopies we develop a structural model for these glasses.

2. Experimental

2.1. Sample preparation and characterization

Glass samples were obtained in 10 g batches by melt quenching methodology using tungsten (VI) oxide (99.8%, Alfa Aesar), sodium metaphosphate (96% Synth) and sodium fluoride (99%, Riedel-de

* Correspondence to: H. Eckert, São Carlos Institute of Physics, University of São Carlos - USP, São Carlos, SP, Brazil.

** Corresponding author.

E-mail addresses: eckerth@uni-muenster.de (H. Eckert), marcelo.nalin@unesp.br (M. Nalin).

Haën). The powdered compounds were mixed using a Speed Mixer DAC 150.1 FVZ-K from Flack Tek, Inc. Mixtures were heated in a Pt-Au crucible at 400 °C for 1 h. Subsequently, the crucible was covered with a Pt-Au lid to minimize fluoride losses and heated between 900 and 1150 °C for 30 min, depending on the glass composition. The melt was transferred to a pre-heated brass mold kept at 50 °C below the glass transition temperature. The glass was subsequently annealed at this temperature for 5 h, before it was cooled down to room temperature. Differential Scanning Calorimetry (DSC) was carried out using a NETZSCH DSC 404 F3 Pegasus equipment, within Pt crucibles, at a heating rate of 10 °C min⁻¹, in N₂ atmosphere (flow rate 50 mL min⁻¹). Glass transition (T_g) and crystallization (T_c) temperatures were extracted from the onset points of the apparent heat capacity changes with a precision of ± 2 °C.

Temperature dependent ionic conductivities were measured using a SOLARTRON 1296 instrument coupled to a NOVOTHERM furnace. Measurements were done over the frequency range 50 mHz to 10 MHz and the temperature range of 50 to 150 °C. A sample cell holder, ZGS-BDCS-140801 from Novocontrol Technologies, was attached to the instrument and computer interfaced with “WinFit” software for data acquisition. All the samples were polished with SiC and cut into a rectangular shape, before coating all faces with sputtered gold for 180 s using a Q150R Rotary-Pumped Sputter Coater from Quorum Technologies.

Raman spectra were measured at room temperature using a HORIBA Jobin Yvon LabRam HR spectrometer equipped with an OLYMPUS BX41 microscope and a He-Ne 632.8 nm laser. The resolution error was ± 1 cm⁻¹.

2.2. Solid state NMR

All solid-state NMR experiments were carried out at room temperature using a BRUKER Avance III 400WB HD (9.4 T) and an AGILENT DD2 600 spectrometer interfaced with a 5.7 T magnet. ²³Na MAS-NMR spectra were measured at 9.4 T within a 4 mm triple resonance probe at a spinning speed of 14.0 kHz, using small flip angles effected by pulses of 1.0 μs length. 2D- triple-quantum MAS-NMR spectra were measured on the same spectrometer, at a spinning speed of 12.0 kHz, using the three-pulse zero-filtering sequence [16]. The lengths of the strong TQ-excitation and reconversion pulse as directly optimized on the samples were 6.8 and 2.4 μs, respectively, at a power level of 250 W, followed by a 10 μs detection pulse at a power level of 7 W. 196 data points were acquired in the t_1 domain, incremented by 7.14 μs, and signal-averaged with 180 scans, using a relaxation delay of 2 s. ³¹P MAS-NMR spectra were measured with the same equipment, using $\pi/2$ pulses of 3.4 μs length and a recycle delay of 300 s. In a separate set of experiments, the scalar-coupling-based one-dimensional refocused INADEQUATE sequence [17] was applied to select only those ³¹P nuclei involved in the P-O-P connectivity, whereas isolated P species are filtered out by appropriate phase cycling. Spinning rates and pulse lengths were identical to those chosen for the MAS experiments and double quantum coherence was created during a mixing time of 16.6 ms corresponding to a ²J(³¹P-³¹P) coupling constant of 30 Hz. ¹⁹F MAS NMR spectra were measured at 5.7 T, in 3.2 mm rotors spinning at 25.0 kHz, using a rotor-synchronized Hahn-echo sequence with 4 rotor cycles for the echo formation in order to remove the probe background signal. Different evolution times were tested and the values used in the experiments do not influence the relative intensities of the resolved spectral components, indicating similar spin-spin relaxation times. 90° pulses of 1.5 μs length and relaxation delays of 50 s were used. Chemical shifts are reported relative to 1 M aqueous NaCl solution, 85% H₃PO₄, and liquid CFCl₃ using solid NaCl, BPO₄, and AlF₃ as a secondary references (7.4 ppm, -29.3 ppm, and -172 ppm for ²³Na, ³¹P, and ¹⁹F, respectively). Rotational Echo Double Resonance (REDOR) [18] experiments were conducted using the methodology and parameters described in the Supporting Materials Section. In all of the

REDOR experiments, π pulse lengths on the recoupling channel were adjusted by maximizing the REDOR difference signal ΔS at a chosen dephasing time. As described in detail in the Supporting Materials Section, the data were analyzed in terms of dipolar second moments $fM_{2(S-I)}$, using a parabolic fit to the data within the initial data range $\Delta S/S_0 \leq 0.2$ [19],

$$\frac{\Delta S}{S_0} = \frac{4}{3\pi^2} (NT_r)^2 f M_{2(S-I)} \quad (1)$$

where NT_r , the number of rotor cycles times the rotor period defines the dipolar mixing time, and f is a calibration factor to be determined by studies on a suitable model compound having similar spin dynamics as the glasses under study.

In the case of the ³¹P{²³Na} REDOR experiments a different pulse sequence and analysis method was used [20], as described in detail in the Supporting Information Section. For all the measurements the $M_{2(S-I)}$ values contain information about the distribution of internuclear distances r_{Si} , according to the van Vleck expression [21]:

$$M_{2(S-I)} = \frac{4}{15} \left(\frac{\mu_0}{4\pi} \right)^2 I(I+1) \gamma_I^2 \gamma_S^2 \hbar^2 N^{-1} \sum_I \frac{1}{r_{Si}^6} \quad (2)$$

In Eq. (2) N is the number of S-spins for which $M_{2(S-I)}$ is being calculated. This method was used to obtain the experimental calibration factors on the model compounds Na₂PO₃F [22] and NaWO₂PO₄ [23], for which the distance distribution is known from the crystal structures. In various of such measurements, signals for individual crystallographic sites can be resolved, for which then individual second moments can be measured, which were then used to obtain averaged calibration factors f .

3. Results and discussion

3.1. Glass formation and physical properties

Fig. 1 summarizes the results of a systematic exploration of glass formation within the WO₃-NaPO₃-NaF ternary. Within the large vitreous domain observed, we selected the cross-section (WO₃)_x(NaPO₃)_{30-x}(NaF)_{70-x} (with $30 \leq x \leq 70$ at constant NaPO₃ content) for detailed structural study. The set of glass compositions chosen for this study (Fig. 1) corresponds to the glasses having the highest stability (resistance against crystallization) as evidenced from differential scanning

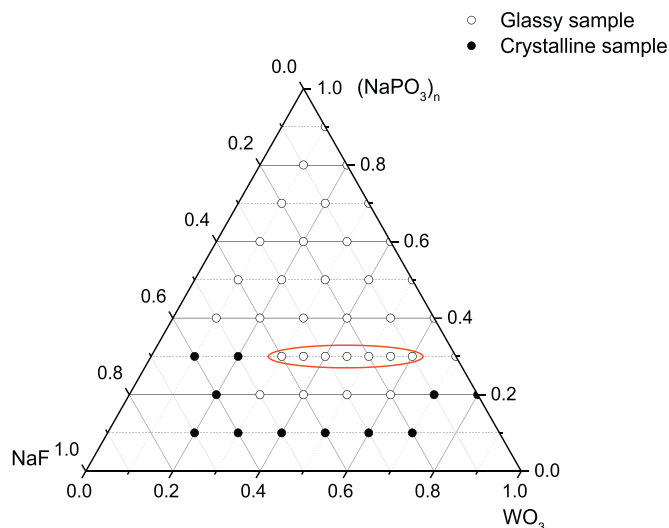


Fig. 1. Ternary composition diagram of the WO₃-NaPO₃-NaF glass system. Samples circled in red denote the samples studied in this work. (For interpretation of the references to colour in this figure legend, the reader is referred to the web version of this article.)

Table 1
Characteristic temperatures and thermal stabilities of x WO₃-30 NaPO₃ - (70- x) NaF glasses.

Sample	Characteristic temperatures (°C)		
	T_g (± 2 °C)	T_x (± 2 °C)	$T_x - T_g$ (± 2 °C)
W30	356	–	> 200
W35	379	–	> 200
W40	401	–	> 200
W45	420	–	> 200
W50	469	623	154
W55	477	600	123
W60	508	602	104

calorimetry (see Fig. S2).

Table 1 summarizes the characteristic temperatures and the thermal stabilities, $T_g - T_x$. T_g increases linearly with increasing WO₃ content suggesting that WO₃ serves to cross-link the one-dimensional phosphate chains by P-O-W bonds, as previously documented for other tungsten phosphate [6] and fluorophosphate glass systems [2,3]. When compared with the T_g values of binary NaPO₃-WO₃ glasses having the same WO₃/NaPO₃ ratios, the data indicate that NaF consistently decreases T_g , proportional to its content. This result indicates that NaF serves as a network modifier in the present system, lowering the degree of polymerization by decreasing the number of bridging oxygen atoms. In addition, our results show that NaF tends to increase the thermal stabilities of these glasses, with values of $T_x - T_g$ larger than 200 °C at the highest NaF contents studied. Such conditions facilitate the preparation of large samples without crystallization and of optical fibers. Fig. 2 shows that with increasing WO₃ content the samples turn increasingly dark colored, presumably because of the formation of some W⁵⁺ ions [6]. The evolution of the optical absorption spectra is summarized in Fig. 2, showing a progressive shift of the UV absorption band edge towards higher wavelengths as the WO₃ content increases. For the samples with the highest W contents, a d-d transition band assigned to pentavalent tungsten species is observed near 585 nm.

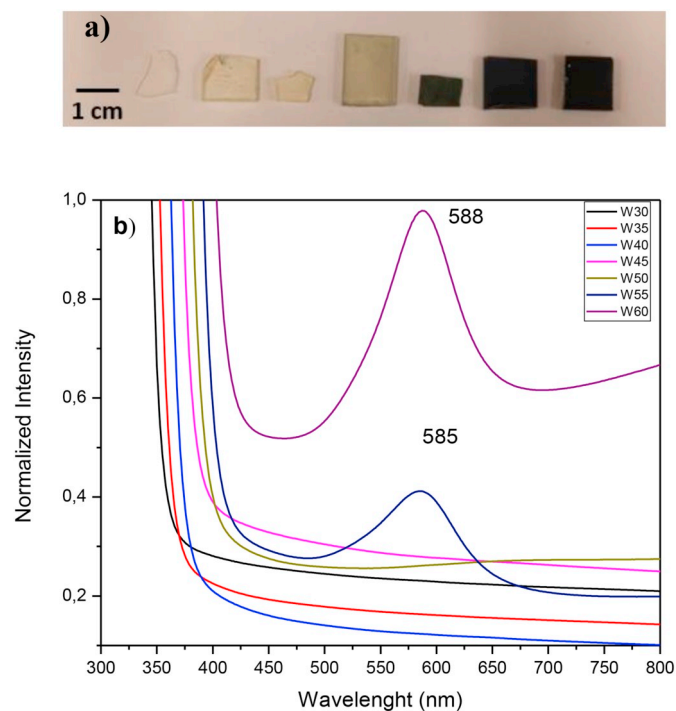


Fig. 2. Photograph of the samples (a), from left to right W30, W35, W40, W45, W50 and W60. UV-Vis Absorbance spectra (b) of the glasses at room temperature. All curves were normalized by the respective sample thickness.

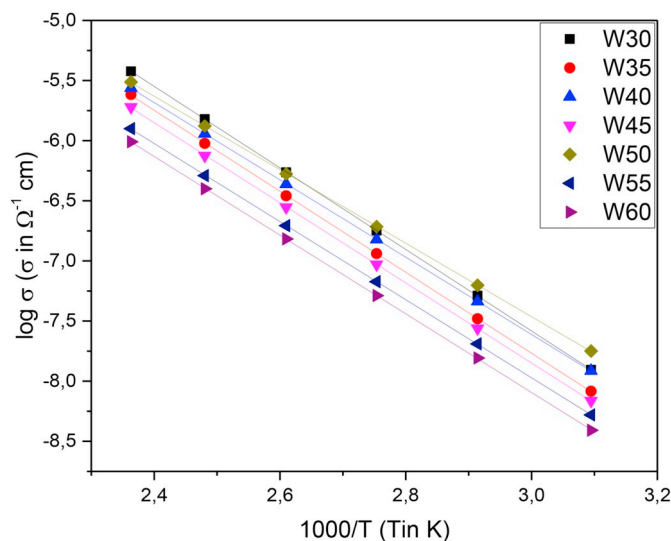


Fig. 3. Temperature dependence of bulk ionic conductivity of W30, W35, W40, W45, W50, W55 and W60 glasses. All the samples have Arrhenius response. Solid curves are linear regression fits to each data set. Errors are represented by symbol sizes. Linear regression fits of all the data sets have coefficients of correlation higher than 0.99990.

3.2. Electrical conductivities

The temperature dependence of the electrical conductivity is shown in Fig. 3. All the glasses follow Arrhenius behavior and, with the exception of the high-tungsten content glasses, show similar temperature dependences. Table 2 presents the activation energies, E_a , the pre-exponential factors of the Arrhenius expression, σ_0 , and the electrical conductivities at 300 K, σ_{300} . While the electrical conductivities of the glasses with the higher NaF contents tend to be higher than those of the glasses with the lower NaF contents, there is a considerable amount of scatter. There is no clear correlation of the activation energies E_a with composition, but the pre-exponential factors σ_0 decrease systematically with increasing x , resulting in a one-order-of-magnitude difference between glass W30 and glass W60. This latter result suggests that with increasing WO₃ contents the electrical conductivities measured in this glass series are increasingly influenced by an electronic contribution related to the W⁵⁺ \rightarrow W⁶⁺ electron hopping process evident in Fig. 2. Thus, we attribute the weak dependence of E_a on x and the absence of a correlation of σ_{300} with the concentration of sodium ions to opposite compositional trends of the ionic and electronic conductivity contributions in these glasses. Additional details of these measurements are reported in the Supporting Information Section.

Table 2

Room temperature (300 K) electrical conductivities σ_{300} , activation energies E_a and pre-exponential factors σ_0 measured for the glasses.

Sample	E_a (eV \pm 0.01 eV) ^a	σ_0 ($\Omega^{-1} \text{cm}^{-1}$)	σ_{300} ($10^{-9} \Omega^{-1} \text{cm}^{-1}$) ^b
W30	0.67	388	1.94
W35	0.67	217	1.29
W40	0.64	107	2.07
W45	0.66	139	1.10
W50	0.61	50	3.29
W55	0.64	59	0.88
W60	0.65	52	0.65

^a The mathematical error of activation energy given by linear regression is lower than 0.01. Therefore, we rounded up the error to two decimal cases to assure a realistic physical uncertainty.

^b The generally accepted value for a typical uncertainty in electrical conductivity measurements by impedance spectroscopy (IS) is between 3 and 5%. [24].

3.3. Raman spectra

Fig. 4 summarizes the Raman spectra of the glasses and some reference compounds in the ternary system. Crystalline $(\text{NaPO}_3)_n$ presents two main bands at 680 and 1160 cm^{-1} , attributed to the symmetric P-O-P stretching mode, ν_{ss} , and the O-P-O stretching mode of metaphosphate-type $\text{Q}^{(2)}$ units, respectively. WO_3 has two bands at 806 and 717 cm^{-1} , attributed to asymmetric and symmetric stretching of W-O-W bonds respectively, while Na_2WO_4 shows only the asymmetric and symmetric stretching modes of terminal W-O bonds, at 926 and 810 cm^{-1} respectively [25]. The Raman spectrum of $\text{Na}_2\text{PO}_3\text{F}$ shows peaks at 1006 and 1022 cm^{-1} , assigned to the P-O stretching mode in the PO_3F^{2-} group. Deformation modes involving P-O and P-F bonds are observed in the range of $545\text{--}550 \text{ cm}^{-1}$.

Vibrational mode assignments for all the glass samples are summarized in Table 3 [6]. At the low frequency end, two broad, but relatively distinct features, centered at 250 and 370 cm^{-1} , can be observed at all glass compositions, including fluoride-free samples. We thus attribute them to bending modes involving W-O and W-F linkages. Careful inspection of the spectra reveals that the band at 370 cm^{-1} increases in intensity with increasing NaF content (see Supporting

Table 3

Wave numbers ($\pm 1 \text{ cm}^{-1}$) measured for the major features observed in the Raman spectra and their assignments to vibrational modes following refs [6–9].

Peak Number	Wave number (cm^{-1})							Vibrational mode
	W30	W35	W40	W45	W50	W55	W60	
1	234	240	244	222	228	214	228	$\delta(\text{PO}_4)_{\text{Td}}$
2	287	295	287	280	280	268	287	$\delta(\text{WO}_6)_{\text{Oh}}$
3	382	382	380	380	380	378	375	$\nu(\text{W-F})$; $\nu(\text{F-PO}_3)$
4	488	480	500	502	470	494	492	$\nu(\text{W-F})$
5	552	552	551	550	549	554	554	$\delta(\text{P-F})$ in O-P-F
6	593	601	600	597	594	598	593	$\delta(\text{P-O})$ in O-P-F
7	633	637	635	637	634	634	643	$\delta_{\text{as}}(\text{PO}_4)$
8	755	775	775	780	740	697	697	$\nu_{\text{s}}(\text{W-O-W})$
9	820	830	832	838	837	828	812	$\nu_{\text{as}}(\text{W-O-W})$
10	909	914	920	931	935	948	951	$\nu(\text{P-O})$ in $\text{PO}_4\text{-WO}_6$
11	937	945	946	954	954	962	967	$\nu(\text{W-O})$ in WO_6 units
12	1085	1076	1069	1051	1060	1047	1038	$\nu_{\text{as}}(\text{PO}_4)$
13	1183	1192	1191	1207	1185	1204	1195	$\nu(\text{P-O})$

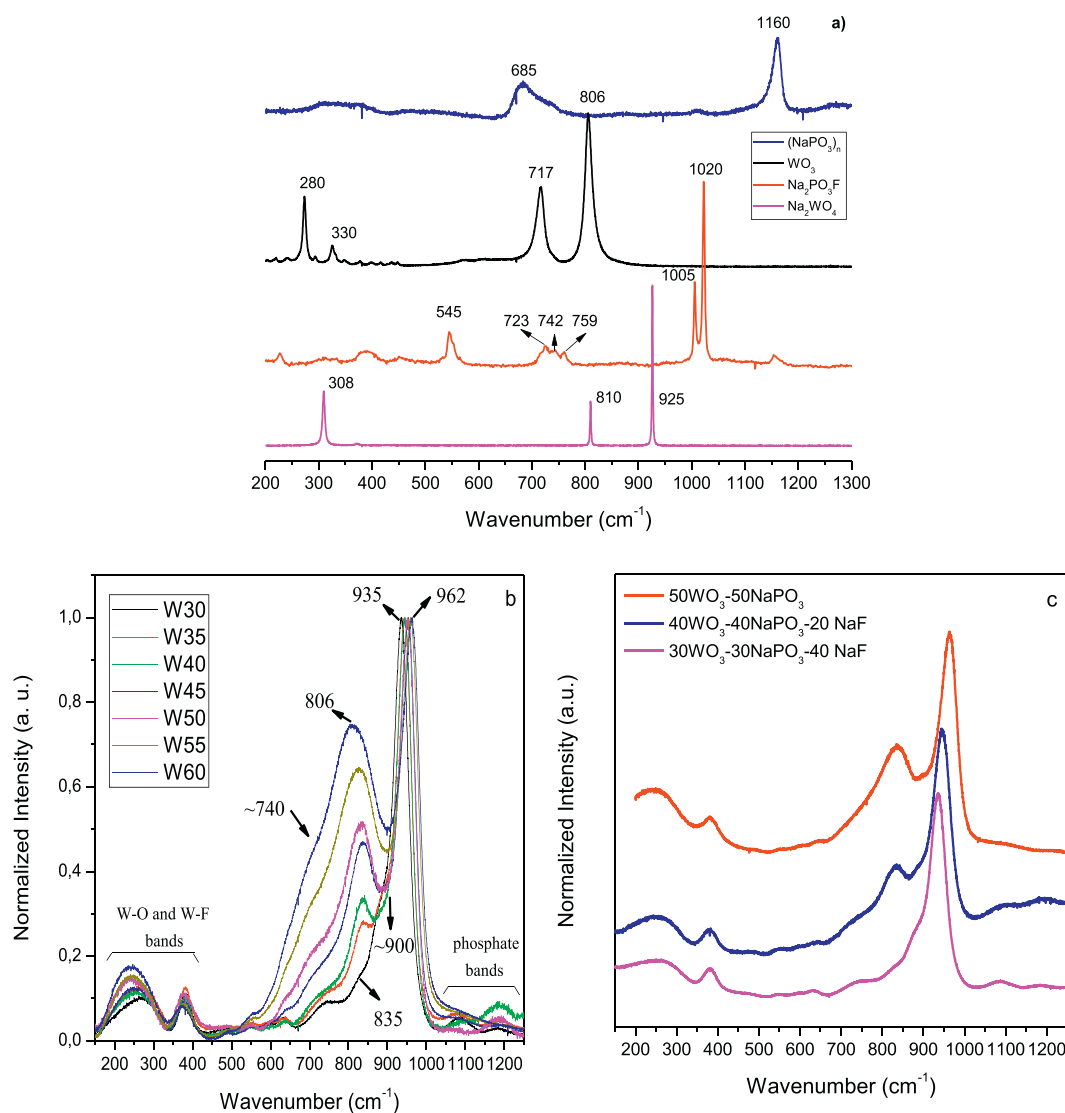


Fig. 4. Raman spectra of model compounds (a) and the glasses under study (b). Part c of the figure shows the progressive decrease of the area ratio $A_{\nu_{\text{as}}(\text{W-O-W})}/A_{\nu(\text{W-O})}$ in another set of glasses with increasing NaF content at a fixed $\text{WO}_3/\text{NaPO}_3$ ratio of one.

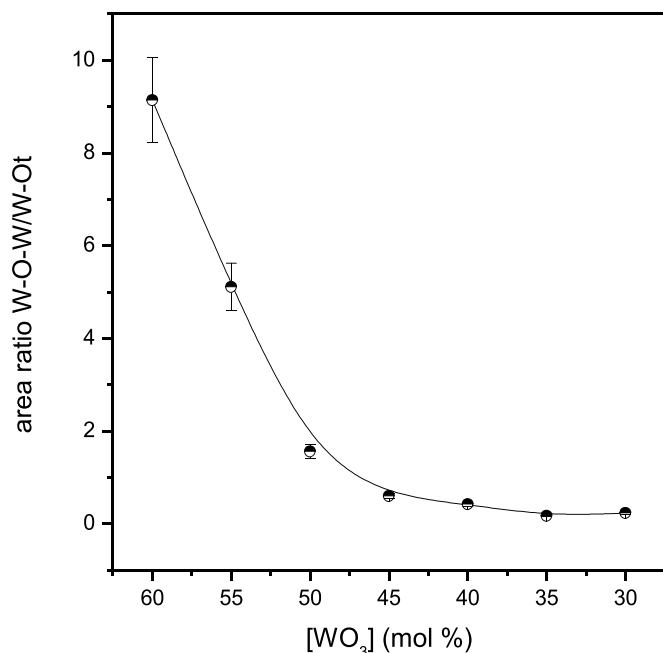


Fig. 5. Area ratio $A(\nu_{as}(W-O-W))/A(\nu(W-O_t))$ as a function of x in glasses with compositions x WO_3 -30 $NaPO_3$ - $(70-x)$ NaF . Solid curve represents a guide to the eyes.

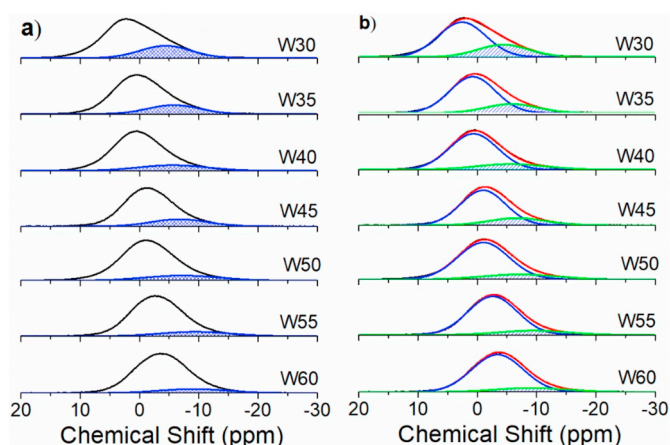


Fig. 6. ^{31}P MAS-NMR spectra of the glasses under study. (a) Superposition of the single-pulse (black curves) and the 1D- Refocused INADEQUATE spectra (blue-shaded curves), b) proposed deconvolution model.

Table 4

^{31}P isotropic chemical shift values δ_{CS}^{iso} and relative areas A of the individual $Q_{mW}^{(n)}$ phosphate species, determined from the deconvolution of the single pulse ^{31}P MAS-NMR spectra and isotropic chemical shifts and $SOQE$ parameters obtained from simulations of the ^{23}Na MAS-NMR spectra using the Czjzek model [27] (a) and TQMAS-NMR (b) [16].

Sample	$Q_{mW}^{(0)}$		$Q_{mW}^{(1)}$		SOQE (± 0.1 MHz)		$\delta_{CS}^{iso}(^{23}Na)$ (± 1 ppm)	
	δ_{iso} (± 0.5 ppm)	A ($\pm 2\%$)	δ_{iso} (± 0.5 ppm)	A ($\pm 2\%$)	a	b	a	b
W30	2.6	70	-4.4	30	2.3	1.8	-9	-7
W35	0.8	76	-5.8	24	2.3	2.1	-10	-7
W40	0.6	79	-5.6	21	2.2	2.2	-12	-8
W45	-1.0	78	-6.7	22	2.1	2.1	-14	-11
W50	-1.1	86	-7.1	14	2.1	2.1	-15	-12
W55	-2.6	85	-9.4	15	2.1	2.1	-16	-14
W60	-3.4	86	-9.1	14	2.0	2.1	-17	-14
W70	-4.7	79	-10.8	21	2.0	1.9	-17	-16
$NaPO_4WO_2$	0.0/-2.0	100	-	-	-	-	-	-

^a From fit to MAS spectra.

^b From TQMAS analysis.

Materials), leading to the suggestion that vibrations involving F-bonded tungsten species make a strong contribution to this peak. Further support for this assignment comes from the Raman spectrum of the chiolite-type crystal $Na_5W_3O_9F_5$, which features a band around 350 – 450 cm^{-1} assigned to vibrations of WX_6 octahedra ($X = O, F$) [26].

The bottom part of Fig. 4 summarizes the results obtained for the glasses. The features near 740 and 806 – 830 cm^{-1} are assigned to vibrations involving W-O-W linkages, whereas the sharper band, which shifts from 937 to 966 cm^{-1} with increasing WO_3 content, is attributed to vibrations involving W-O terminal bonds and bridging oxygen atoms within P-O-W linkages. The spectral features of the latter are evident in the Raman spectrum of the model compound $NaWO_2PO_4$, whose structure is based on PO_4 units linking to four WO_6 octahedra [23]. Using a deconvolution procedure, we determined the relative areas of the two Raman bands near 830 cm^{-1} (W-O-W bond vibration) and near 930 cm^{-1} ($W-O_t$ stretching mode and W-O-P bond vibration). Fig. 5 indicates that the area ratio $A(\nu_{as}(W-O-W))/A(\nu(W-O_t))$ systematically decreases with increasing NaF content, suggesting a progressive disappearance of the W-O-W linkages. This conclusion is further strengthened by Fig. 4c, bottom, which compares the Raman spectrum of the NaF-richest glass, $30WO_3$ - $30NaPO_3$ - 40 NaF , with those of two additional glasses, $50WO_3$ - $50NaPO_3$, and $40WO_3$ - $40NaPO_3$ - $20NaF$, which are not part of this study. In these three glasses, which have a fixed $WO_3/NaPO_3$ ratio of one, the network modifier role of NaF in breaking W-O-W linkages, diminishing the band intensity near 830 cm^{-1} is clearly evident. Alongside the trend observed in Figs. 4 and 5, the dark coloration of the glasses also vanishes. The resulting network modified by NaF is more ionic and less connected, accounting for the decrease of T_g values with increasing NaF modifier content.

3.4. High-resolution solid state NMR

3.4.1. ^{31}P MAS-NMR

The single-pulse ^{31}P MAS-NMR spectra (Fig. 6) are broad and poorly resolved, suggesting a wide distribution of local environments. The successful deconvolution of these spectra is based on the 1D-refocused INADEQUATE NMR experiments, which selectively detect only those ^{31}P nuclei involved in P-O-P linkages. These species appear at distinctly lower frequencies than the majority of the phosphate units (see Fig. 6a). While the two-component deconvolution is probably a simplification it is the only one that can be rationalized on the basis of the data available. In principle, multiple phosphate units having different numbers of non-bridging oxygen atoms, and P-O-P and P-O-W connectivities may be expected. We categorize them in terms of $Q_{mW}^{(n)}$ terminology, where n represents the number of P-O-P linkages, while m denotes the number of tungsten species linked to the phosphate group ($m + n \leq 4$). The two

principal contributions differentiated in Fig. 6 include: a minority of $Q_{mW}^{(1)}$ units and a majority of $Q_{mW}^{(0)}$ units, which goes undetected in the refocused INADEQUATE experiment. Table 4 summarizes the corresponding lineshape parameters and the $Q_{mW}^{(1)}$ - and $Q_{mW}^{(0)}$ fractional areas (in %), where the concentration of $Q(1)$ units is seen to decrease with increasing WO_3 content. The compositional evolution observed in the ^{31}P MAS-NMR spectra in the present system is analogous to the one observed in the fluoride-free $NaPO_3-WO_3$ system [6], where it reflects the conversion of P-O-P into P-O-W linkages eventually resulting in the $Q_{4W}^{(0)}$ units that are also found in crystalline $NaWO_2PO_4$ [23].

No further differentiation of phosphorus species could be achieved on the basis of either $^{31}P\{^{19}F\}$ or $^{31}P\{^{23}Na\}$ REDOR data, indicating that the corresponding heteronuclear dipole-dipole interaction strengths (and hence their relative distance distributions) are comparable for all of the P species present.

3.4.2. ^{23}Na MAS- and TQMAS-NMR

Fig. 7 summarizes the ^{23}Na MAS-NMR spectra. Asymmetric lineshapes typical of a wide distribution of nuclear electric quadrupolar coupling constants are observed. Analysis of these data on the basis of a Czjzek distribution [27] implemented within the DMfit program [28] yielded average values of the isotropic chemical shifts and SOQE parameters as listed in Table 4. Listed alongside these values are data obtained from TQMAS NMR. While there is a slight discrepancy between both sets of data (which may be caused by the very different modes of analyzing them), they show consistently that the strength of the average ^{23}Na quadrupolar coupling is independent of composition, while there is a definitive trend of increasing chemical shift with increasing NaF content. Using $^{23}Na\{^{19}F\}$ REDOR experiments on representative glasses, we did not detect any systematic chemical shift difference between Na species bonded to fluoride ions and those not bonded to fluoride ions. Based on this finding, we conclude that the ^{23}Na chemical shift trend evident in Table 4 is not due to an increasing amount of fluoride ions in the first coordination sphere of the sodium ion, but rather reflects a general trend of ^{23}Na chemical shifts to become more positive with increasing overall Na content, as a result of more

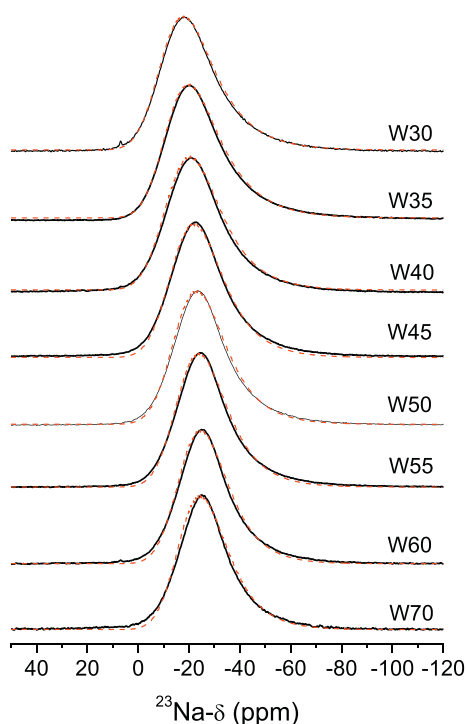


Fig. 7. ^{23}Na MAS-NMR spectra of the glasses under study (black curves). Red curves represent simulations of the data using the Czjzek model [27].

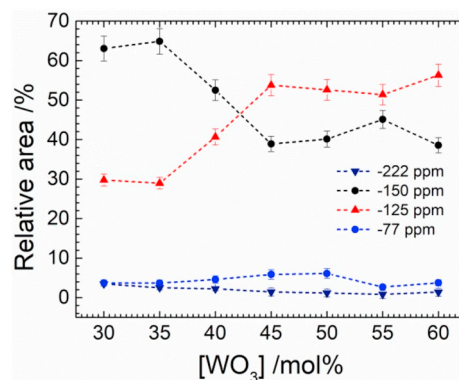
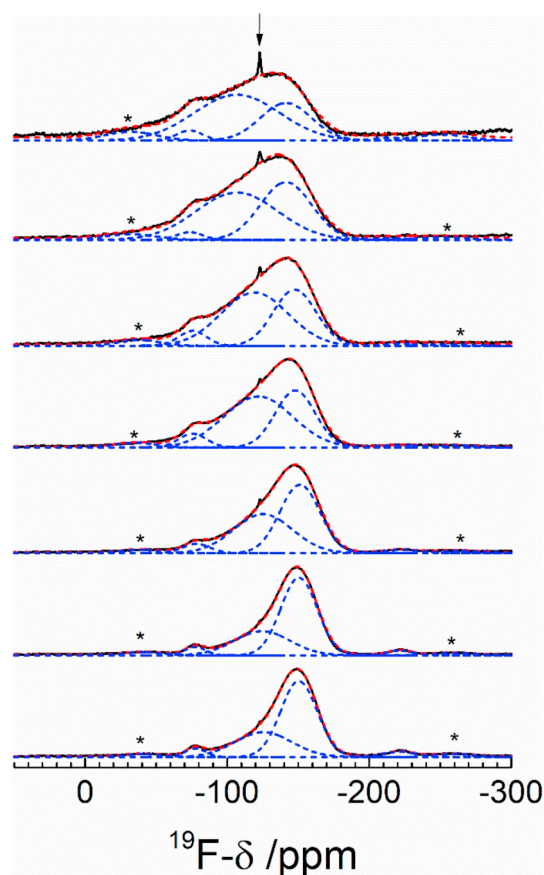


Fig. 8. Top: - Solid state ^{19}F MAS NMR spectra of the studied glasses (black curves). Deconvolutions of the experimental data are shown as dashed curves. The arrow indicates the position of the peak belonging to the probe background signal. Spinning sidebands are marked with asterisks. Bottom: - Relative areas of the components of the deconvolutions as a function of the WO_3 concentration. Errors are estimated on the basis of value changes observed upon fitting with different parameter constraints. Dashed lines are linear connections between data points.

covalence due to Na-O-Na contacts [29].

3.4.3. ^{19}F MAS-NMR

The ^{19}F MAS-NMR spectra (Fig. 8) indicate four distinct components at around -75 ppm, -125 ppm, -150 ppm and -222 ppm. The signal at -75 ppm can be attributed to P-bound F species ($F_{1P}^{(1)}$), as confirmed by $^{19}F\{^{31}P\}$ REDOR data shown below. The line at -222 ppm can be assigned to F species within NaF clusters, F_{Na} , as indicated both by its chemical shift and its rapid dephasing behavior in $^{19}F\{^{23}Na\}$ experiments. Both of these species make only rather minor contributions to

Table 5

^{19}F isotropic chemical shifts (in ppm vs CFCl_3) and fractional areas A (in %) of the individual spectral components, determined from the deconvolution of the single pulse ^{19}F MAS-NMR spectra. Errors in are estimated on the basis of value changes observed upon fitting with different parameter constraints.

Sample	$F_{1P}^{(1)}$		$F_{1W}^{(1)-(2)}$		$F_{1W}^{(1)-(1)}$		F_{Na}	
	$\delta_{iso} (\pm 0.1)$	$A (\pm 10\%)$	$\delta_{iso} (\pm 0.5)$	$A (\pm 5\%)$	$\delta_{iso} (\pm 0.5)$	$A (\pm 5\%)$	$\delta_{iso} (\pm 0.5)$	$A (\pm 10\%)$
W30	-77.6	3.5	-125.5	30	-150.5	63	-221.3	3.5
W35	-77.4	3.7	-124.7	29	-150.5	65	-221.5	2.4
W40	-78.3	4.6	-125.2	40	-151.2	53	-222.7	2.2
W45	-75.6	5.9	-121.8	54	-148.0	39	-223.7	1.4
W50	-75.6	6.5	-119.2	53	-147.4	40	-	-
W55	-73.6	3.0	-106.8	52	-141.4	45	-	-
W60	-73.6	3.8	-106.8	56	-141.4	39	-	-

the overall fluoride inventory. The by far dominating fluoride species gives rise to an asymmetric lineshape within the -100 to -180 ppm spectral region. It can be deconvoluted in terms of two distinct components near -120 and -150 ppm, whose ratio shows a systematic compositional evolution (see Table 5). The $^{19}\text{F}\{^{31}\text{P}\}$ and $^{19}\text{F}\{^{23}\text{Na}\}$ REDOR data (to be discussed further below) reveal that both fluoride species have similar spatial proximities to phosphate or fluoride ions. In view of this result it seems unlikely that these two components reflect fluoride species in separate microphases. As will be justified further below, we may attribute them to terminal fluoride species ($F^{(1)}$) bound to one tungsten unit each, which are of two different types: one of them, denoted $F_{1W}^{(1)-(1)}$ and observed at -150 ppm, can be assigned to an F species bound to octahedral tungsten units exclusively linked to phosphate species, whereas the other component, denoted $F_{1W}^{(1)-(2)}$ and observed at -120 ppm, is assigned to an F species bound to an octahedral tungsten unit that is involved in W-O-W bonding.

3.4.4. High resolution dipolar NMR

Results from the six double resonance experiments are summarized

in Figs. 9–17, and the corresponding dipolar second moments, corrected by model compound calibration are collected in Table 6. The calibration compounds used are NaWO_2PO_4 for the $^{23}\text{Na}/^{31}\text{P}$ REDOR experiments, and $\text{Na}_2\text{PO}_3\text{F}$ for the $^{23}\text{Na}/^{19}\text{F}$ and the $^{31}\text{P}/^{19}\text{F}$ REDOR experiments. Concerning the latter combination of nuclei, the calibration remains problematic, however, as the dipole-dipole coupling in the model compound (having a P-F bond) is significantly stronger than in the glasses. As a matter of fact, no reliable calibration was possible in the case of the $^{31}\text{P}\{^{19}\text{F}\}$ REDOR experiment because of the extremely rapid dephasing observed. For this reason, uncorrected $M_{2(P-F)}$ values are listed in Table 6. All the values fulfill the criterion [30]

$$\frac{M_{2(S-I)}}{M_{2(I-S)}} = \frac{I(I+1)[I]}{S(S+1)[S]} \quad (3)$$

within experimental error limits, where $[I]$ and $[S]$ are the concentrations of the I and S nuclear species under consideration. Based on this criterion, we consider the measurement results and the calibration procedure generally reliable, possibly with the exception of the $^{31}\text{P}\{^{19}\text{F}\}$ REDOR results for which no calibration is available.

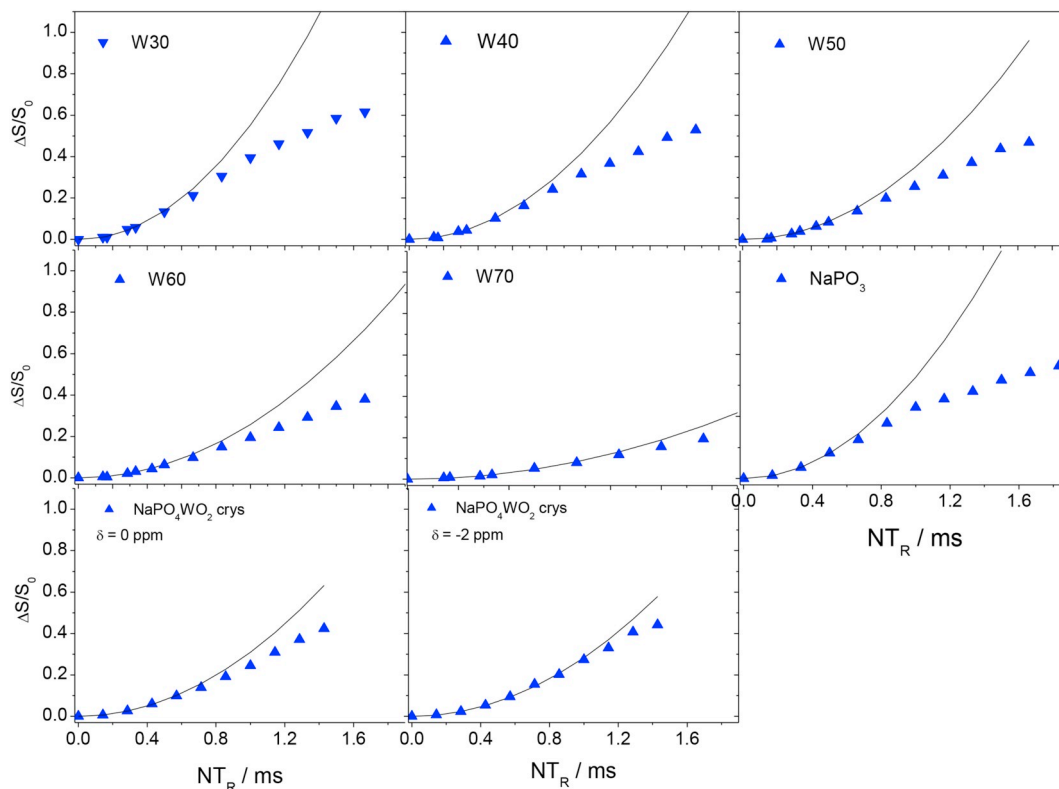


Fig. 9. $^{31}\text{P}\{^{23}\text{Na}\}$ REDOR curves of glass samples and the crystalline reference compounds, NaPO_3 and NaPO_4WO_2 . Solid curves are parabolic fits to Eq. (1), analyzed within the data range $\Delta S/S_0 \leq 0.2$.

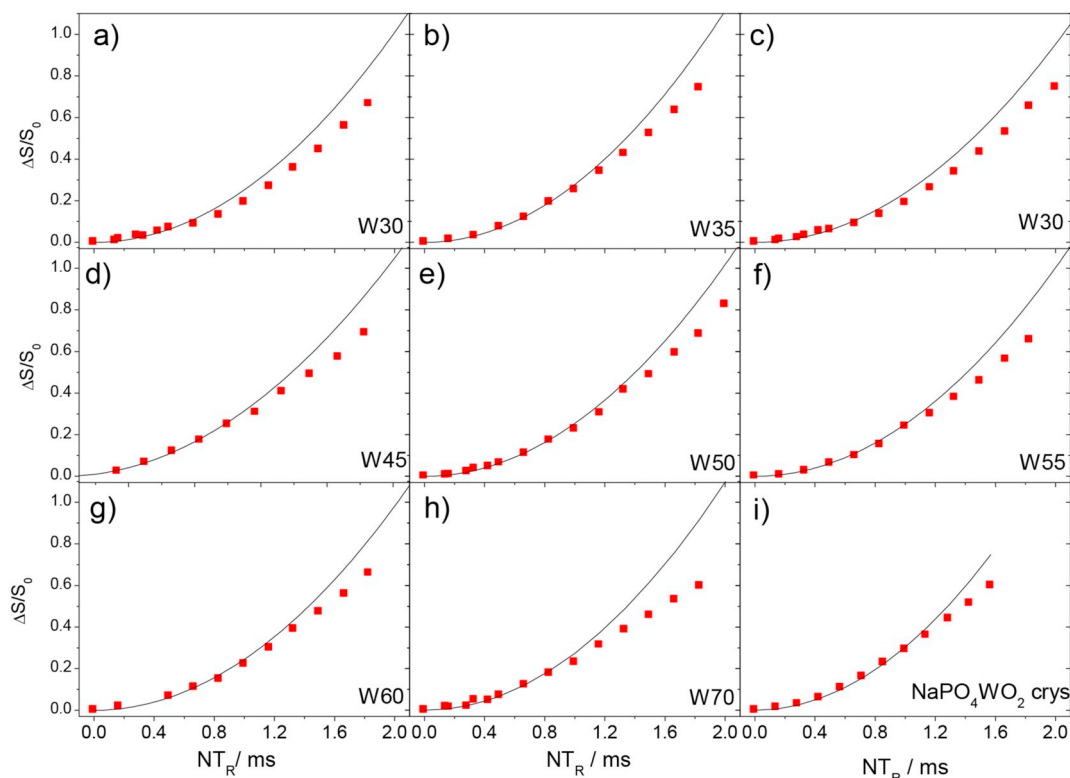


Fig. 10. $^{23}\text{Na}\{^{31}\text{P}\}$ REDOR curves of a) W30, b) W35, c) W40, d) W45, e) W50, f) W55, g) W60, h) W70 glass samples and i) NaPO_4WO_2 crystalline compound. Solid curves are parabolic fits to Eq. (1), analyzed within the data range $\Delta S/S_0 \leq 0.2$.

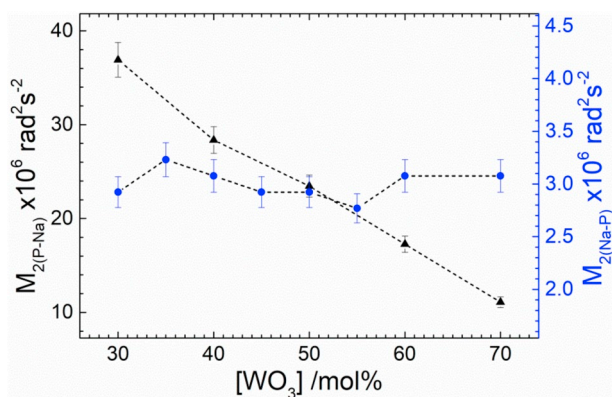
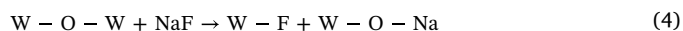


Fig. 11. Second moments $M_{2(\text{P-Na})}$ and $M_{2(\text{Na-P})}$ obtained respectively from $^{31}\text{P}\{^{23}\text{Na}\}$ and $^{23}\text{Na}\{^{31}\text{P}\}$ REDOR studies as a function of composition. Data points are connected by dashed lines.

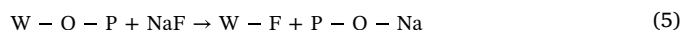
We can now discuss the compositional evolution of the relative Na/P -, Na/F -, and P/F spatial proximities. Fig. 8 shows the $^{31}\text{P}\{^{23}\text{Na}\}$ REDOR data. Clearly, $M_{2(\text{P-Na})}$ decreases with decreasing NaF content, as the Na/P ratio changes from 2.33 in the W30 sample to 1.0 in the W70 sample. As confirmed by the ^{31}P MAS-NMR spectra the major structural change associated with this evolution is the gradual disappearance of anionic phosphate species with Na-O-P proximities towards the formation of a local orthophosphate unit linked to WO_6 octahedra as realized in the model compound NaWO_2PO_4 . The second moment $M_{2(\text{P-Na})}$ in this material is significantly smaller than in NaPO_3 , owing to the significantly longer average $\text{Na}\cdots\text{P}$ distances. In contrast, an entirely different compositional behavior is seen in the $^{23}\text{Na}\{^{31}\text{P}\}$ REDOR curves (Fig. 10). Even though the P/Na ratio increases from 0.42 (in W30) to 1.0 (in W70), there is no concomitant increase in $M_{2(\text{Na-P})}$; this value remains essentially independent of composition (see

Fig. 11). In agreement with the trends in $M_{2(\text{P-Na})}$ discussed above we can conclude that this observation reflects two mutually compensating effects. While at high NaF contents there is significant participation of fluoride in the first coordination sphere of the Na^+ ions, which thus have fewer phosphate species to be found there, these phosphate species do interact more effectively with the sodium ions than in those glasses with low NaF content, where the W-bonded orthophosphate units $\text{Q}_{4\text{W}}^{(0)}$ dominate, from which the sodium ions are generally more remote. This assertion is nicely confirmed by the $^{23}\text{Na}\{^{19}\text{F}\}$ REDOR data shown in Fig. 12. As expected, $M_{2(\text{Na-F})}$ shows a monotonic linear trend (with some noise), decreasing from $55.0 \times 10^6 \text{ rad}^2\text{s}^{-2}$ for the W30 sample ($\text{F/Na} = 0.57$) towards $7.5 \times 10^6 \text{ rad}^2\text{s}^{-2}$ for the W60 sample. Most interestingly Fig. 12 reveals that for the low-NaF samples W50, W55, and W60 the $^{23}\text{Na}\{^{19}\text{F}\}$ REDOR data show bimodal behavior, consisting of a minor fraction of Na species (about 40, 30, and 20%) interacting with F and a major fraction of Na species that are quite remote from fluoride and therefore do not contribute to REDOR dephasing. This result corresponds with a model in which the NaF exclusively breaks W-O-W linkages according to the melt reaction.



While the fluoride ions associated with these W-F bonds can be assumed to be in proximity of the sodium ions of the W-O-Na fragments, they can be considered more remote from the Na ions compensating the charges of the $\text{Q}_{4\text{W}}^{(0)}$ phosphate component. If we assume such a preferential modification model, we expect the fraction of Na ions close to F to be 40%, 33%, and 25% in these three high- WO_3 glasses, in very good agreement with the experimental findings.

For the glasses with higher NaF contents we also have to consider the modification of the W-O-P linkages, which may be described by the reaction model.



In this case, the fluoride species involved in this process are

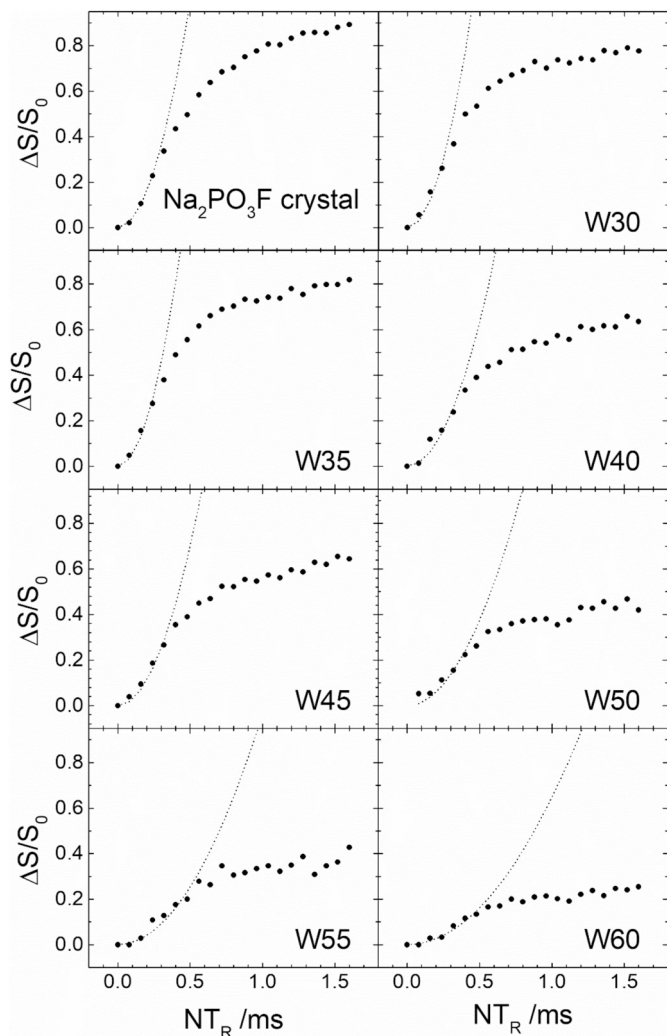


Fig. 12. $^{23}\text{Na}\{^{19}\text{F}\}$ REDOR dephasing curves for the studied glasses. Dotted curves are parabolic fits to eq. (1), analyzed within the data range $\Delta S/S_0 \leq 0.2$.

expected to be in proximity of the sodium ions that are interacting with the $Q_{3W}^{(0)}$ species, and therefore, no more bimodal behavior is expected (and detected) anymore. Of course, an increase of $M_{2(\text{Na-F})}$ with increasing NaF content is already expected purely on the basis of the fact that the F/Na ratio in the glass increases from 0.25 in the W60 sample to 0.57 in the W30 sample. In this connection the most significant result we observe is the **anti-correlation** of $M_{2(\text{F-Na})}$ with the Na/F ratio within this series: these values actually **decrease** (from $543 \times 10^6 \text{ rad}^2\text{s}^{-2}$ in W30 towards $176 \times 10^6 \text{ rad}^2\text{s}^{-2}$ in W60 even though the Na/F ratio **increases** from 1.75 to 4.0 along that series. As relationship (3) is maintained over the entire range of compositions, an error in this measurement can be ruled out. Again, this result indicates that in the glasses with low NaF contents the fluoride species are in very different chemical environments and rather remote from the majority of the sodium ions. While the latter are still associated with the $Q_{4W}^{(0)}$ species, the major part of the fluoride species are remote from sodium, and associated with W-octahedra involved in W-O-W bonding. This assignment is re-enforced by the $^{19}\text{F}\{^{31}\text{P}\}$ REDOR data summarized in Fig. 15. Again, $M_{2(\text{F-P})}$ is **anti-correlated** with the P/F ratio, showing a decrease by 30% even though the P/F ratio increases from 0.75 in W30

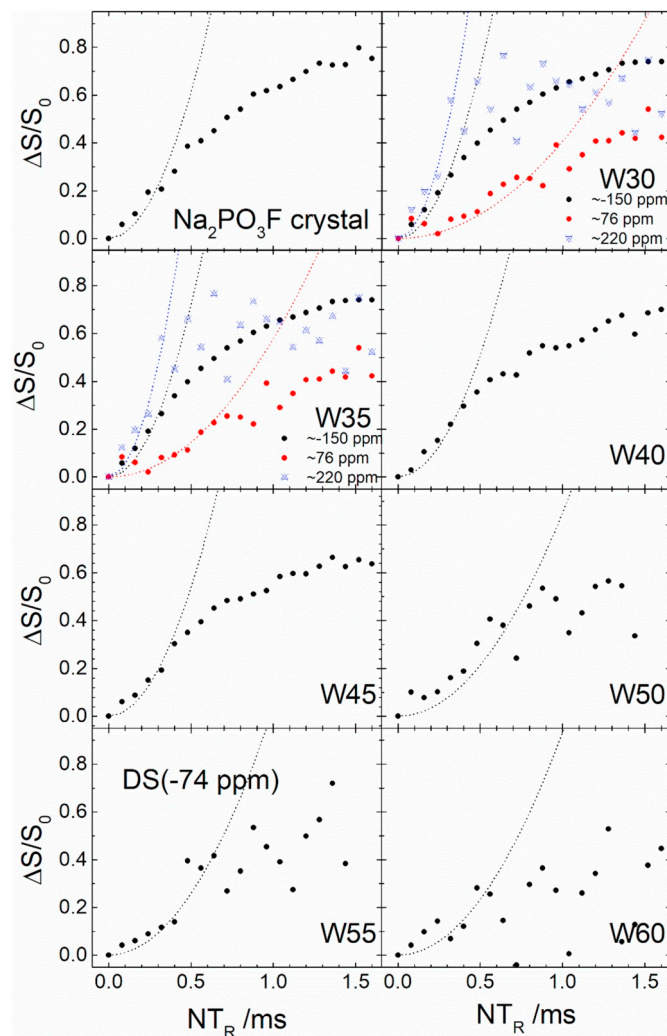


Fig. 13. $^{19}\text{F}\{^{23}\text{Na}\}$ REDOR dephasing curves for different regions of the ^{19}F NMR spectrum obtained for the studied samples and for crystalline $\text{Na}_2\text{PO}_3\text{F}$. Dotted curves are parabolic fits to eq. (1), analyzed within the data range $\Delta S/S_0 \leq 0.2$.

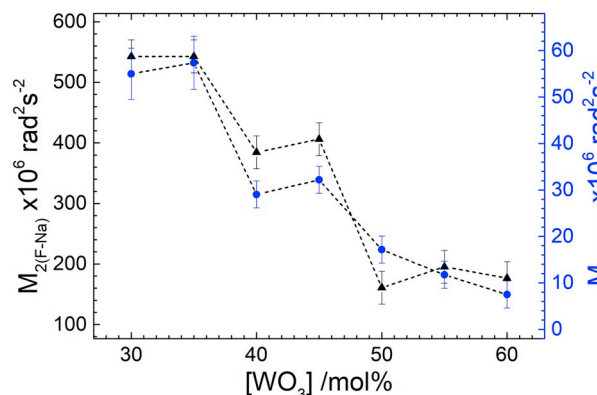


Fig. 14. Second moments $M_{2(\text{F-Na})}$ and $M_{2(\text{Na-F})}$ obtained for the ^{19}F nuclei contributing to the signals at -120 and -150 ppm and the entire inventory of the ^{23}Na nuclei, respectively. Data points are connected by dashed lines.

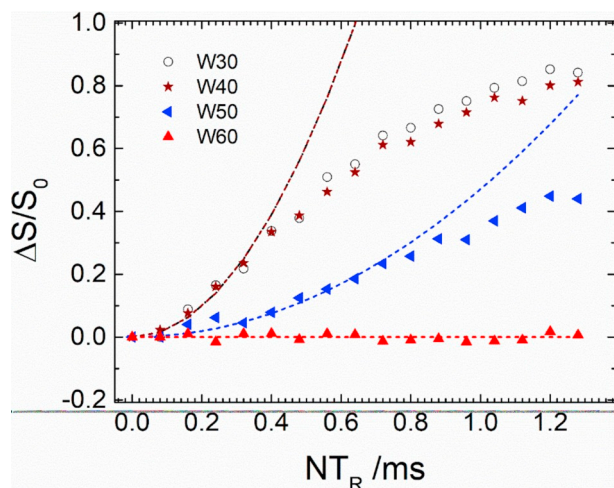


Fig. 15. $^{31}\text{P}\{^{19}\text{F}\}$ REDOR dephasing curves for selected glasses. Dashed curves are parabolic fits to eq. (1), analyzed within the data range $\Delta S/S_0 \leq 0.2$.

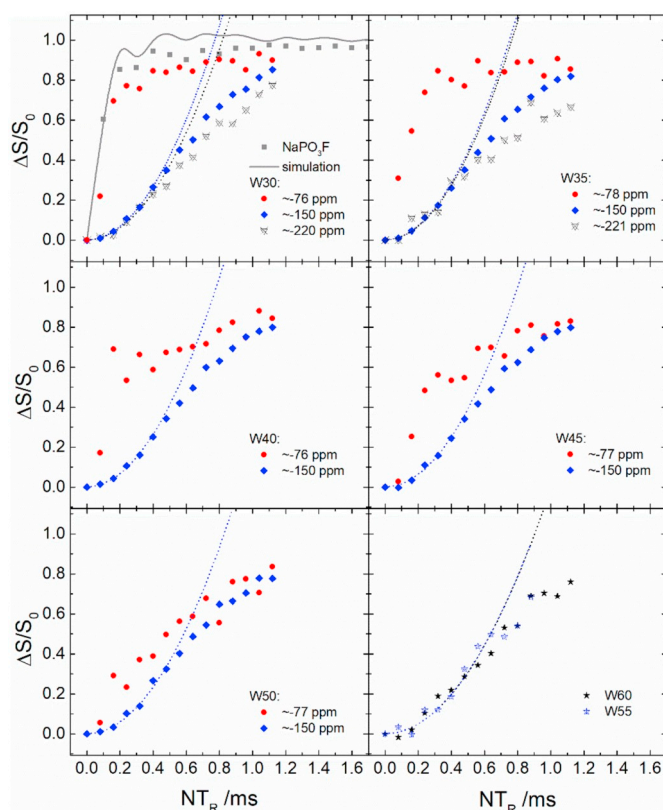


Fig. 16. $^{19}\text{F}\{^{31}\text{P}\}$ REDOR dephasing curves for different regions of the ^{19}F NMR spectrum obtained for the glasses studied and for crystalline $\text{Na}_2\text{PO}_3\text{F}$. Where possible, separate REDOR curves were analyzed for resolved sites. Dephasing is particularly rapid for the -77 ppm signal, which arises from F-bonded P species. The F species near -120 and -150 ppm could not be differentiated; only a REDOR result comprising both species is available here. Errors are reflected by symbol sizes. Dashed curves are parabolic fits to eq.(1), analyzed within the data range $\Delta S/S_0 \leq 0.2$. The solid curve represents a SIMPSON simulation considering a two spin system with an effective second moment calculated from the $\text{Na}_2\text{PO}_3\text{F}$ crystal structure.

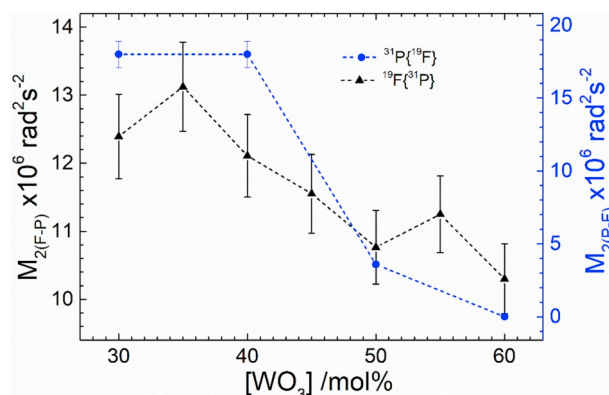


Fig. 17. Compositional dependence of $M_{2(\text{F-P})}$ and $M_{2(\text{P-F})}$ obtained for the ^{19}F nuclei contributing to the signals at -120 and -150 ppm and for the entire inventory of the ^{31}P nuclei, respectively. Data points are connected by dashed lines.

towards 3.0 in W60. The substantial change in the spatial distribution of P relative to F also becomes very clear in the $^{31}\text{P}\{^{19}\text{F}\}$ REDOR data of the samples W50 and W60, showing that in these two samples the F and P species are very distant from each other.

Finally, we note that the systematic changes in the fluoride speciation are also seen in the deconvoluted ^{19}F MAS-NMR spectra (Fig. 8). At high WO_3 contents the signal near -120 ppm is the dominant one. This confirms our assignment to W-bonded F species that arise from the network modification reaction (4). The W-atoms these fluoride species are bonded to still contain additional W-O-W linkages. In contrast the signal near -150 ppm, which dominates the spectrum at high NaF contents, is attributed to W-bonded F species that arise from network modification reaction (5). The W atoms these fluoride species are bonded to do not contain any W-O-W linkages. Evidently the ^{19}F chemical shift is sensitive to the coordination state of the tungsten species to which they are bonded.

4. Conclusions

Glasses in the ternary system $x \text{WO}_3 - 30 \text{NaPO}_3 - (70-x) \text{NaF}$ ($30 \leq x \leq 70$) were prepared, and their physical properties discussed in relation to structural information obtained via NMR and Raman spectroscopies. Substitution of the WO_3 by the NaF component produces no clear effects on the room temperature electrical conductivities and activation energies. A systematic trend observed in the Arrhenius pre-exponential factor suggests that with increasing WO_3 contents the electrical conductivities measured in this glass series are increasingly influenced by an electronic contribution. This contribution is likely related to the $\text{W}^{5+} \rightarrow \text{W}^{6+}$ electron hopping process evident from the optical absorption spectra. The structure of the binary $\text{NaPO}_3\text{-WO}_3$ glasses is dominated by WO_6 units that are cross-linked by $\text{Q}_{4\text{W}}^{(0)}$ orthophosphate groups. Depending on the $\text{WO}_3/\text{NaPO}_3$ ratio one also finds P-O-P linkages of the $\text{Q}^{(1)}$ type and WO_6 groups linked to each other via W-O-W linkages. Incorporation of NaF into such glasses tends to decrease the glass transition temperatures, suggesting that it adopts a network modifier role. Indeed both Raman scattering and solid state NMR results indicate that NaF decreases the network connectivity by breaking W-O-W and W-O-P linkages with formation of W-F terminal bonds. In glasses containing low NaF contents, the fluoride ions interact rather weakly with the phosphate units. This finding suggests that the breakage of W-O-W linkages is the preferred network modification

Table 6

Heteronuclear dipolar second moments measured from REDOR experiments on different sets of nuclei in the glasses and in crystalline model compounds. Asterisks indicate raw values fM_2 obtained directly from Eq. (1); numbers directly below indicate M_2 values after calibration using the tabulated calibration factor f . Error estimates are based on the changes in fitting parameter caused by variation of the data range used in fitting the data to Eq. (1).

M_2 ($\times 10^6 \text{rad}^2 \text{s}^{-2}$)		W30	W35	W40	W45	W50	W55	W60	W70	$\text{Na}_2\text{PO}_3\text{F}$	NaPO_4WO_2	f
$^{31}\text{P}\{^{23}\text{Na}\}$ ($\pm 10\%$)	Theo.									47.5 / 51.7	20.5 / 14.7	0.55
	Exp.	20.3*		15.6*		12.9*		9.5*	6.1*	n.m.	11.6* / 7.6*	
$^{23}\text{Na}\{^{31}\text{P}\}$ ($\pm 10\%$)	Theo.									6.07 / 5.50 / 3.92 / 4.35	2.8 / 4.2	0.65
	Exp.	1.9*	2.1*	2.0*	1.9*	1.9*	1.9	1.8*	2.0*	n.m	2.3*	
$^{19}\text{F}\{^{23}\text{Na}\}$ ($\pm 20\%$)	Theo.									485 / 436	–	0.0391
	Exp.	21.2*	21.2*	15.0*	15.9*	6.3*	7.6*	6.9*		18.1*	–	
$^{23}\text{Na}\{^{19}\text{F}\}$ ($\pm 15\%$)	Theo.									60.1 / 60.7 / 12.6 / 50.8	–	0.64
	Exp.	35.2*	36.7*	18.6*	20.6*	11.0*	7.5*	4.8*		29.5*	–	
$^{19}\text{F}\{^{31}\text{P}\}$ ($\pm 10\%$)	Theo.									948 / 1046	–	0.80
	Exp.	9.9*	10.5*	9.7*	9.3*	8.6*	9.0*	8.2*		798*	–	
$^{31}\text{P}\{^{19}\text{F}\}$ ($\pm 10\%$)	Theo.									945 / 1049	–	–
	Exp.	18*		18*		3.6*		0		–	–	

process, which dominates in the glasses with high WO_3 contents. On the other hand, in $\text{NaPO}_3\text{-WO}_3$ glasses having low levels of W-O-W linkages, the breakage of W-O-P linkages becomes the dominant process, resulting in W-F terminal bonds and non-bridging oxygen species attached to phosphorus. The decrease in network connectivity caused by the above-described processes accounts for the experimentally observed decrease in glass transition temperatures with increasing NaF contents.

Acknowledgements

Authors would like to acknowledge the Brazilian funding agencies FAPESP (CEPID Project 2013/07793-6) and CNPq. M.O.Jr acknowledges post-doctoral support by FAPESP, grant number 2013/23490-3. S.S. acknowledges SPEC-FAPESP funding process number 15/22828-6.

Appendix A. Supplementary data

Description of the REDOR methodology as applied in the present study, experimental conditions of the measurements, and model compound calibrations, dynamic scanning calorimetry data, additional analyses from electrical conductivity measurements, Raman deconvolution analyses, ^{23}Na TQMAS NMR spectra. Supplementary data to this article can be found online at <https://doi.org/10.1016/j.jnoncrysol.2018.10.043>.

References

- [1] S.M. Salem, E.K. Abdel-Khalek, E.A. Mohamed, M. Farouk, *J. Alloys Comp.* 513 (2012) 35–43.
- [2] G. Poirier, Y. Messaddeq, S.J.L. Ribeiro, M. Poulain, *J. Solid State Chem.* 178 (2005) 1533–1538.
- [3] G. Poirier, F.C. Cassanjes, Y. Messaddeq, S.J.L. Ribeiro, *J. Non-Cryst. Solids* 355 (2009) 441–446.
- [4] A.M. Ataala-Ahmed, S. Afif, M. Hassan, M. Abdallah, M. Milanov, H.Y. Abboul-Einein, A. Mohamed, *J. Non-Cryst. Solids* 491 (2018) 43–54.
- [5] G. Upender, Ch. Sameera Devi, V. Chandra Mouli, *Mater. Res. Bull.* 47 (2012) 3764–3769.
- [6] C.C. Araujo, W. Strojek, L. Zhang, G. Poirier, S.J.L. Ribeiro, Y. Messaddeq, *J. Mater. Chem.* 16 (2006) 3277–3284.
- [7] N.I. Fernandes, G. Poirier, M. Nalin, *Solid State Ionics* 181 (2010) 1125–1130.
- [8] R.P.R.D. Nardi, C.E. Braz, A.S.S. de Camargo, S.J.L. Ribeiro, L.A. Rocha, F.C. Cassanjes, G.E. Poirier, *Opt. Mater.* 49 (2015) 249–254.
- [9] M. Nalin, G. Poirier, S.J.L. Ribeiro, Y. Messaddeq, L. Cescato, *J. Non-Cryst. Solids* 353 (2007) 1592–1597.
- [10] I. Rösslerová, L. Koudelka, Z. Cernosek, P. Mosner, L. Benek, *J. Non-Cryst. Solids* 384 (2013) 41–46.
- [11] G. Porier, M. Nalin, Y. Messaddeq, S.J.L. Ribeiro, *Solid State Ionics* 178 (2007) 871–875.
- [12] M. Rioux, Y. Ledemi, J. Viens, S. Morency, S. Alireza Ghaffari, Y. Messaddeq, *R. Soc. Chem.* (2015) 1.
- [13] M. Blais-roberge, M. Rioux, Y. Ledemi, Y. Messaddeq, *J. Non-Cryst. Solids* 470 (2017) 61–69.
- [14] M. Rioux, Y. Ledemi, Y. Messaddeq, *J. Non. Cryst. Solids* 459 (2017) 169–175.
- [15] M. Desjardins, M. Roudjane, Y. Ledemi, G. Gagnon-Turcotte, E. Maghsoudloo, G. Filion, B. Gosselin, Y. Messaddeq, *Prog. Biomed. Optics and Imaging - SPIE Proc.* (2018) 104820W.
- [16] A. Medek, J.S. Harwood, L. Frydman, *J. Am. Chem. Soc.* 117 (12) (1995) 779–12,787.
- [17] P. Guerry, M.E. Smith, S.P. Brown, *J. Am. Chem. Soc.* 131 (2009) 11861–11874.
- [18] T. Gullion, J. Schaefer, *J. Magn. Reson.* 81 (1989) 196–200.
- [19] M. Bertmer, H. Eckert, *Solid State Nucl. Magn. Reson.* 15 (1999) 139–152.
- [20] W. Strojek, M. Kalwei, H. Eckert, *J. Phys. Chem. B* 108 (2004) 7061–7073.
- [21] J. H. Van Vleck, 74 (1948), 1168–1183.
- [22] J. Durand, L. Cot, J.L. Galigné, *Acta Crystallogr. B* 30 (1974) 1565–1569.
- [23] P. Kierkegaard, *Arkiv Kemi* 18 (1962) 553–575 1962).
- [24] S. Lanfredi, L. Dessemond, A.C.M. Rodrigues, *J. Am. Ceram. Soc.* 86 (2003) 291–298.
- [25] F. Dhikhali, S. Megdiche Borchani, M. Rasheed, S. Barille, S. Shihab, K. Guidara, M. Megdishe, *R. Soc. open sci* 5 (172) (2018) 214.
- [26] M. Couzi, P. Rocquet, J.P. Chaminade, J. Ravez, *Ferroelectrics* 80 (1988) 113–116.
- [27] J.B.D. Espinose de Lacaillerie, C. Fretigny, D. Massiot, *J. Magn. Reson.* 192 (2008) 244–251.
- [28] D. Massiot, F. Fayon, M. Capron, I. King, S. Le Calve, J. Alonso, J.O. Durand, B. Bujoli, Z. Gan, G. Hoatson, *Magn. Reson. Chem.* 40 (2001) 70–76.
- [29] H. Eckert, *Z. Phys. Chem.* 224 (2010) 1591–1653.
- [30] B. Stevansson, R. Matthew, Y. Yu, M. Eden, *J. Magn. Reson.* 251 (2015) 52–56.